Coalescence-induced jumping of microdroplets on superhydrophobic surfaces – A numerical study

Citation for the original published paper (version of record):
Konstantinidis, K., Göhl, J., Mark, A. et al (2022). Coalescence-induced jumping of microdroplets on superhydrophobic surfaces – A numerical study. Canadian Journal of Chemical Engineering, 100(12, Special Issue Article): 3517-3530. http://dx.doi.org/10.1002/cjce.24591

Received: 28 February 2022 | Revised: 7 April 2022 | Accepted: 11 April 2022
DOI: 10.1002/cjce.24591

SPECIAL ISSUE ARTICLE

THE CANADIAN JOURNAL OF CHEMICAL ENGINEERING

Coalescence-induced jumping of microdroplets on superhydrophobic surfaces—A numerical study

Konstantinos Konstantinidis[1] | **Johan Göhl**[2] | **Andreas Mark**[2] | **Srdjan Sasic**[1]

[1]Department of Mechanics and Maritime Sciences, Division of Fluid Dynamics, Chalmers University of Technology, Gothenburg, Sweden

[2]Fraunhofer-Chalmers Centre, Chalmers Science Park, Gothenburg, Sweden

Correspondence
Konstantinos Konstantinidis, Department of Mechanics and Maritime Sciences, Division of Fluid Dynamics, Chalmers University of Technology, Gothenburg, 41296, Sweden.
Email: konkonst@chalmers.se

Funding information
Swedish National Infrastructure for Computing (SNIC); Swedish Research Council, Grant/Award Numbers: 2018-05973, 2019-04969

Abstract

We develop a numerical framework for simulating the coalescence and jumping of microdroplets on superhydrophobic surfaces. The framework combines the volume of fluid (VOF) method with models for advancing and receding contact angles on a number of superhydrophobic surfaces. We demonstrate the temporal and spatial convergence of the framework and show agreement between our numerical results and other experimental studies. The capillary-inertial scaling is investigated together with the existence of a cut-off behaviour frequently observed in the lower size-range of that regime. We investigate findings in some of the previous studies that the cut-off behaviour can be attributed to viscosity effects and dissipation due to interaction with surface microstructures. We exemplify specific features related to the jumping process and the corresponding energy budget analysis when microdroplets coalesce and jump. We have tested droplets of a radius as small as 0.5 μm that are still jumping but recorded a decrease in the jumping velocity and the degree of energy conversion compared to the jumping of larger droplets. We argue and prove that strong capillary forces originating from the high curvature oscillations dissipate the energy of the system significantly faster in the case of microdroplets.

KEYWORDS

contact angle, microdroplets, VOF–immersed boundary, wetting

1 | INTRODUCTION

The phenomenon of droplets jumping upon coalescence on superhydrophobic surfaces has been relatively recently observed.[1] It immediately attracted considerable research focus, as no external energy is required in order for the droplets to jump. The driving force behind the process is the combination of strong capillary forces, which are present during coalescence, and low adhesion to the surface, which is observed in the case of superhydrophobic surfaces.[2] The research activity related to jumping droplets has been steadily increasing for the last decade, with applications being found in, among others, anti-icing and defrosting technologies,[3–6] heat transfer from drop-wise condensation,[7,8] and various self-cleaning mechanisms.[9–12] Those technological applications are often inspired by mechanisms that have been observed in nature and that aim at providing benefits for animals and plants, such as water-repellency or self-cleaning.[13] Suitable examples in that manner are the lotus leaf[14,15] and the cicada wings.[16]

Coalescence and jumping of droplets on superhydrophobic surfaces have been investigated both experimentally and numerically. Studies agree that the properties of surface microstructures[17,18] or the number of coalescing droplets[19,20] are important factors in determining both the likelihood and the overall efficiency of the entire process. The jumping velocity follows the so-called capillary-inertial scaling law for droplet sizes where gravity can be deemed negligible.[1,2] Furthermore, while experimental studies have often demonstrated the necessity of having high droplet–surface contact angles for the jumping to take place, less attention has been paid to the influence of the hysteresis between the advancing and receding angles. In most cases, such hysteresis has been minimal.[17] A decrease in the value of the contact angle or an increase in the hysteresis causes the contact behaviour to change from a Cassie–Baxter to a partial Wenzel wetting one and a consequent impediment of jumping.[18] The Young's equation determines the ideal equilibrium state in which the triple contact line settles between gas, liquid, and solid phases.[21] This equation expresses the force acting at the liquid–solid interface, from which the adhesion energy is often calculated. When a droplet moves, a three-phase contact line is formed, and, as a consequence, there is a well-known problem for a chosen numerical framework to overcome the inability of the no-slip boundary condition to correctly represent the contact line movement and the induced stress singularity.[22–24] Various measures have been suggested to overcome this problem, including the so-called slip models and the Navier-slip boundary condition, the most popular among them.[22,25]

Moreover, there have been an increasing number of numerical studies looking at fundamental phenomena and characteristic features of the droplets jumping process.[26,27] Liu et al.[28] identified four stages that the merged droplet experiences during coalescence and jumping: (i) a liquid bridge expansion, (ii) acceleration upon impingement of the liquid bridge on a superhydrophobic surface, (iii) retraction of the merged droplet from the surface until the moment of departure, and (iv) deceleration of the merged droplet in air. Previous numerical studies have also shown that the jumping velocity follows the capillary-inertial scaling law.[28,29] These studies predicted jumping of droplets for even higher Ohnesorge numbers than did the early experimental works.[1] Here, it is worth noting that various multiphase flow frameworks have been used to study the jumping of droplets. A number of them have used continuum-based methods that focus on tracking or capturing the interface movement,[29–32] volume of fluid (VOF) probably being the most frequently used among them.[33–36] Surface tension is treated as a body force at the location of the interface, which categorizes VOF as a sharp-interface method. Using VOF, Wasserfal et al.[37] calculated 6% as the degree of energy conversion, the latter being defined as the amount of the released surface energy related to the kinetic energy, and also mentioned a reduction of that value when unequal droplets coalesce. Attarzadeh and Dolatabadi[38] looked at the jumping of droplets when the microstructures on a superhydrophobic surface were of sizes comparable to water droplets of around 20 μm. In addition to continuum-based frameworks, the meso-scale Lattice-Boltzmann approach has also been frequently used[26,39,40] to capture the jumping droplets process, with similar phenomena and stages of the process identified as in continuum-based simulations. Lastly, there have been studies using molecular dynamics (MD) simulations, focusing on molecular interactions of the droplets, the surrounding air, and the superhydrophobic surface.[41–43] The mentioned works dealt with nanodroplets of the radius of up to 50 nm. The observed behaviour of even small droplets was generally in line with that obtained using the continuum-based approaches with larger droplets.

The focus in most studies dealing with jumping droplets has so far been on those with a radius greater than 10 μm, see, for example, works of Boreyko and Chen, Nam et al. and Wen et al.[1,30,44] However, recent numerical and experimental studies have shown that jumping can occur for much smaller droplets of radii as small as 5, 1, or even 0.5 μm.[2,45–47] We term such droplets microdroplets, and they represent the main focus of this work. Microdroplets are of interest in numerous applications, such as those dealing with heat transfer rates through drop-wise condensation[48] and surfaces with antifogging abilities.[49] In the experimental works of Cha et al.[45] and Mulroe et al.,[46] the authors argued that the biggest obstacle for microdroplets to jump is due to the size of microstructures on superhydrophobic surfaces and their arrangement pattern on the top of such surfaces. On the other hand, there are both experimental[46] and numerical works[28,29,37] that confirm the jumping of droplets of sizes less than 1 μm, and, as it will be seen in what follows, the present work also corroborates such observations. Note that one of the difficulties in the experimental studies involving microdroplets can be a technical limitation in the frame rate when capturing the moment of jumping. In addition, the observed deviations for microdroplets in the velocity scaling from the capillary-inertial regime are usually attributed to an increase in the viscous dissipation.[1,50] As a result, the mentioned behaviour is explained by introducing a viscous cut-off region, above which the capillary-inertial law holds. This argument has been challenged as mentioned previously, with adhesion forces due to surface microstructures being considered of greater importance.[51,52]

Although the concept of a critical (minimum) size for a droplet to jump has been discussed before, there is still a lack of a systematic presentation of how the process of jumping takes place for microdroplets (those ranging from 500 nm to 10 μm will be the main focus of this work). The present paper thus aims at filling this gap, by formulating a comprehensive and trustworthy numerical framework that is thoroughly validated and has full control of the numerical aspects of the simulation process. We use a combined immersed boundary–VOF framework, accompanied by a dynamic contact-angle model, to investigate in detail and with sufficient resolution all the stages of the microdroplets jumping process. Such an approach is justified since experimental observations of these phenomena can be hindered by the small time scales of the process and whose capturing may become a significant challenge. Consequently, the goals of the present numerical simulations are (i) to find out whether microdroplets are able to jump at all upon coalescence on a number of tested superhydrophobic surfaces, (ii) to look into the details of the liquid–solid interaction and how the latter affects the jumping process, and finally, (iii) to investigate whether the observed capillary-inertial scaling law for larger droplets still holds for microdroplets, in comparison to experimental data (and the reasons for possible deviations). We do this by controlling both numerical and physical aspects that may cause variations in the jumping itself, the jumping velocity, and the energy conversion process that makes the upwards movement possible.

2 | METHODS

We make use of a combined immersed boundary–VOF method, implemented in our in-house code IPS IBOFlow®.[53] VOF is a single-fluid method that solves the incompressible Navier–Stokes equations

$$\nabla\cdot\mathbf{v}=0,$$
$$\frac{\partial(\rho\mathbf{v})}{\partial t}+\mathbf{v}\cdot\nabla(\rho\mathbf{v})=-\nabla p+\nabla\cdot(\mu\nabla\mathbf{v})+\rho\mathbf{g}+\mathbf{f}_{SF}, \tag{1}$$

where $\mathbf{v}$ represents the velocity field, P is the pressure, $\mathbf{g}$ is the gravitational acceleration, $\mathbf{f}_{SF}$ is the surface tension force at the interface, ρ is the density, and μ is the dynamic viscosity. In order to track the interface location, a transport equation for the volume fraction is solved additionally, which reads as follows

$$\frac{\partial\alpha}{\partial t}+\mathbf{v}\cdot\nabla\alpha=0, \tag{2}$$

where α is the volume fraction. The density and dynamic viscosity are volume averaged at the interface location, wherever a cell is partly occupied by the two fluids.

To model the surface tension, the continuum surface force (CSF) method[54] is used. A body force $\mathbf{f}_{SF}$ that is calculated for a computational cell at the interface is given as

$$\mathbf{f}_{SF}=\sigma\kappa\mathbf{n}, \tag{3}$$

where σ is the surface tension, $\mathbf{n}$ is the interface normal vector, and κ is the interface curvature.

The curvature is obtained by taking the divergence of the interface unit normal vector $\hat{\mathbf{n}}$ as

$$\kappa=-\nabla\cdot\hat{\mathbf{n}}=-\nabla\cdot\left(\frac{\mathbf{n}}{\|\mathbf{n}\|}\right), \tag{4}$$

where the interface normal vector $\mathbf{n}$ in the centre of a cell is calculated from the gradient of the volume fraction field as $\mathbf{n}=\nabla\alpha$.

Adaptive mesh refinement is utilized in the neighbouring regions of the interface and the solid surface. For the latter, the refinement is limited to the region of the surface around which the droplets are placed, in order to reduce the computational cost. Adaptive mesh refinement is implemented with a dynamically refined octree mesh, which has been used in our previous works.[53,55] The velocity and pressure fields are coupled with the help of the segregated semi-implicit method for pressure linked equations-consistent (SIMPLEC) algorithm.[56]

Additionally, we have implemented a balanced-force method,[57,58] which modifies the Rhie–Chow interpolation for face velocities[59] in co-located grid arrangements. The method accounts for the presence of surface tension when interpolating the velocities at the faces in order to reduce spurious currents and prevent pressure oscillations. It achieves that by improving the balance between surface tension and pressure gradient forces.

The solid surface is modelled by triangulated objects and the mirroring immersed boundary method.[53,60] The method is second-order accurate and is used to impose the local boundary conditions. It also enhances the surface force calculations by including the local boundary normal in the contact angle calculations.[55] A Navier-slip boundary condition is used to remove the stress singularity. The velocity of the liquid at the wall is given by

$$\mathbf{v}_{\mathrm{wall}}=\lambda\frac{\partial\mathbf{v}}{\partial n_{\mathrm{w}}}\bigg|_{\mathrm{wall}}, \tag{5}$$

where $\mathbf{v}_{\text{wall}}$ is the slip velocity at the wall, n_{w} is the normal direction to the wall, and λ is the slip length, understood as the distance from the boundary location to the hypothetical no-slip point. We calculate the slip velocity in the tangential direction and set it by the immersed boundary condition at the solid boundary.

Finally, the contact angle is implemented according to Göhl et al.[55] where a dynamic contact angle is imposed depending on whether the contact line is advancing or receding.

3 | VALIDATION OF OUR NUMERICAL FRAMEWORK

In this section, we wish to demonstrate and confirm the ability of our numerical framework to reproduce all fundamental features of the actual jumping process. Special attention is paid to identifying the exact movement of the interface and the corresponding forces. Moreover, we want to outline the difficulties and limitations encountered by all numerical frameworks when capturing the actual movement of the three-phase contact line and the corresponding dynamics of the contact angle. There is an additional challenge in correctly capturing the adhesion of droplets to the superhydrophobic surface and the changes in the behaviour of the contact line when the real geometry of the surface is considered.

The contact angle hysteresis is important in this process, and we focus more on that problem in what follows. In a previous study, Göhl et al.[55] successfully implemented and validated in IPS IBOFlow®, a dynamic contact angle framework able to make use of a number of different models for both advancing and receding contact angles. In this work, we use this framework to look specifically at the jumping of microdroplets on surfaces of different wettabilities and demonstrate its ability to recover fundamental features of jumping of larger droplets as well. In all the cases, we report that the framework recreated the conditions of the jumping process with a high accuracy, as the mass of water droplets in the simulations was conserved successfully. In addition, all fluid properties in the simulations were given actual values for a water–air system at 20°C, which corresponds to a density ratio of $\rho_l/\rho_g = 830$, a viscosity ratio of $\mu_l/\mu_g = 55$, and a surface tension of $\sigma = 0.0729$ N/m.

We now demonstrate the temporal and spatial convergence of our simulations. First, we present our motivation for the chosen time step. Two levels of adaptive interface refinements are used on the base grid, giving a minimum cell size of 2.5 μm. The minimum cell size is kept constant for the simulations presented in Figure 1. The time step Δt remained constant throughout each simulation, while the highest Courant number (CFL) number related to each time step varies depending on the maximum velocity. The time step Δt was varied from $2 \cdot 10^{-7}$ s down to $0.5 \cdot 10^{-7}$s. In this test case, the initial droplets have a radius (R) of 100 μm, and the minimum cell size corresponds to 40 cells per radius of the initial droplets, which is the resolution suggested by our grid convergence study. The vertical velocity of the jumping droplet was chosen as the parameter to observe when changing the simulation time step. In Figure 1, this velocity is normalized by the capillary-inertial velocity scale U_{CI}, whereas time is normalized by the capillary-inertial time scale τ_{CI}.

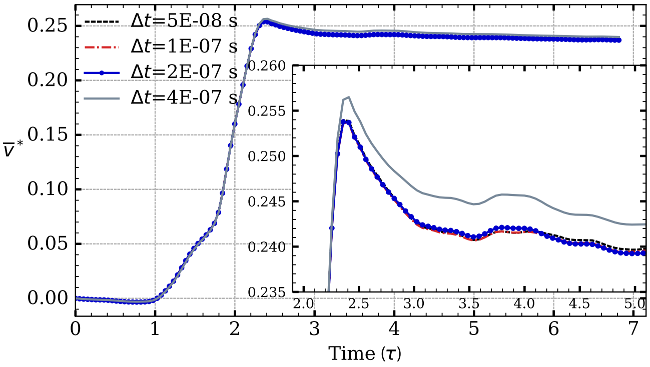

FIGURE 1 Demonstration of time convergence of our simulations. We note that the time convergence is achieved for a time step of $\Delta t = 2 \cdot 10^{-7}$ s or shorter. The initial radius of merging droplets is 100 μm and CFL < 0.7 for the simulation. CFL, Courant number

The largest time step reveals the same evolution of the average velocity as in the initial stage of the simulation. The maximum velocity occurs at $\tau = 2.4$, but the merged droplet detaches itself at an earlier time and it elevates at a higher velocity. The remaining simulations presented in Figure 1 show converged behaviour with respect to the time step. For the simulations with microdroplets, we will use a time step that follows the same principle as the simulation with $\Delta t = 1 \cdot 10^{-7}$ s, where CFL was limited to values below 0.35. However, some adjusting for the different sizes of the droplets in the domain is needed. We want here to accommodate the dependence of the compressive interface capturing scheme for arbitrary meshes (CICSAM) scheme on the CFL value, as this convective scheme relaxes the region of the convective boundness criterion. The scheme is able to accept CFL values of up to unity but switches to a different diffusive scheme for higher CFL values. It needs to be taken into consideration that the velocity is constant when it is normalized for the capillary-inertial regime.

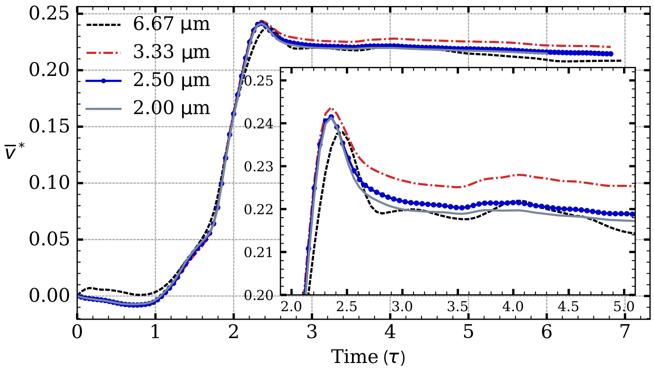

FIGURE 2 Demonstration of spatial convergence of our simulations. Adaptive mesh refinement is utilized, and the minimum cell size is defined. Grid convergence is achieved for a grid of 2.5 μm that corresponds to 40 cells per initial droplet radius. The radius of initial droplets is 100 μm and CFL <0.35 for that simulation. CFL, Courant number

This results in having the same normalized time step $\Delta\tau$ for all such simulations that is given by:

$$\Delta\tau = \Delta t/\tau = \frac{1\cdot 10^{-7}\,\mathrm{s}}{\sqrt{\frac{\rho_l}{\sigma}}R^{\frac{3}{2}}} \simeq 0.051,$$

where $R = 100\ \mu\mathrm{m}$, or similarly

$$\Delta t = 1\cdot 10^{-7}\,(\mathrm{s})\left(\frac{R}{100\,(\mu\mathrm{m})}\right)^{\frac{3}{2}}.$$

To obtain the optimum grid size, we have again looked at the test case of 100 μm droplets. The time step is obtained from the previous time convergence study but adjusted depending on the minimum cell size to keep the same CFL number. The mesh is an octree-mesh, and the size of the cells is adjusted by choosing the base cell size and the number of refinement levels close to the interface. The coarsest grid has a minimum cell size, Δx, of 6.67 μm, which corresponds to a resolution of 15 cells across the initial droplet radius. To look at the required spatial resolution, we have subsequently tested 30 ($\Delta x = 3.33\ \mu\mathrm{m}$), 40 ($\Delta x = 2.5\ \mu\mathrm{m}$), and, finally, 50 ($\Delta x = 2.0\ \mu\mathrm{m}$) cells per R. Figure 2 shows the evolution of the vertical velocity of the system for the different simulations. The inset zooms the events close to the jumping moment and the first oscillations of the merged droplet while being elevated in the air. The Navier-slip boundary condition was used with a given constant slip length l_{sl} of half the length of the cell size, which is $l_{\mathrm{sl}} = 1.0\mu\mathrm{m}$. The slip length of half a cell size is often chosen in similar studies.[61]

In Figure 2, it is revealed that the coarsest grid (shown with the black dashed line) has missed the initial behaviour of the liquid bridge expansion, while it overshoots the moment of the highest velocity, as well as the peak. The remaining grid resolutions have the same evolution of the coalescing stage. In the zoomed-in plot, it is understood that the case of $\Delta x = 3.33\ \mu\mathrm{m}$ has predicted an earlier release from the superhydrophobic surface. Therefore, a greater upwards velocity was preserved during the stage of deceleration, and the droplet jumped with a higher velocity. The two cases of finer refinements showcase the same behaviour throughout the simulation, and the jumping velocity is calculated to be within 0.8% of each other. For these reasons, the spatial resolution of the simulations in the remainder of the article will follow the rule of 40 cells per radius of the initial droplets.

Finally, we continue the validation of our framework by comparing the simulation results with experimental results obtained by another research group. In Figure 3, we present a series of experimentally obtained camera images taken at different instants by Yan et al.,[17] together with the corresponding snapshots from our simulations. The figure depicts the evolution of the process of coalescing and jumping of two equal droplets with a radius of 288 μm, which are placed on a superhydrophobic, nanostructured surface (Yan et al.[17] Figure 1B). The advancing and receding contact angles are $\theta_{\mathrm{adv}} = 170.3^{\circ}$ and $\theta_{\mathrm{rec}} = 167.7^{\circ}$, respectively. The resemblance of the behaviour of the jumping droplets in all the phases of the process is apparent in Figure 3. In the second comparison from the top ($t = 0.29\,\mathrm{ms}$), we show the liquid bridge expansion. The qualitative analysis shows a good agreement between the simulation and the experiment. A slight variation in the times presented can be attributed to possible errors in the image-capturing process. The following two snapshots present the impingement of the liquid bridge on the surface and the formation of an oblate droplet until the point when the contact line starts retracting. We note that we accurately capture the oscillations of the shape of the merged droplet, which have been captured by the experiment. Next, the snapshots at approximately $t \simeq$ 1.4 and 1.6 ms show moments just before and right after the detachment of the merged droplet from the surface. The oscillations are portraying rapid shape changes during the detachment. As a result, the captured image could incorporate a slight distortion, which can be an effect of the limitation imposed by the shutter speed. Nonetheless, we see that the shapes of the merged droplets coincide, with the moment of detachment predicted by our simulation with high precision. Finally, the last two frames present the resulting droplets elevating in the air, depicting similar shape oscillations in the qualitative comparison of the two systems. In

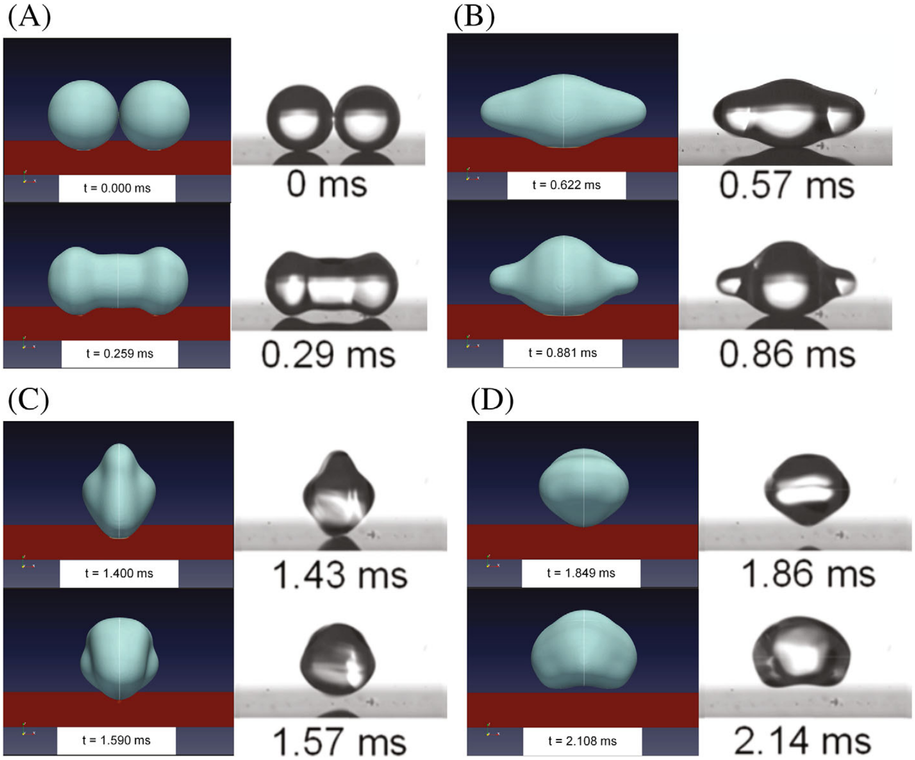

FIGURE 3 Validation by comparing our simulation results with an experiment from Yan et al.[17] Equally sized droplets of an initial radius $R = 288$ μm are presented at different instants throughout the jumping process. The timestamps of the simulation follow the values provided in the experimental study. We observe a high qualitative agreement of the jumping behaviour between our simulation and the experiment.

summary, we argue that the shapes of the droplets and the overall analysis of the jumping process obtained by our simulation highly agree with the published information from the experimental study. This makes it possible for us to now turn our attention to the main topic of our paper, which is the coalescence and jumping of microdroplets on superhydrophobic surfaces.

4 | RESULTS AND DISCUSSION

We first simulate the jumping of 1 μm microdroplets and present the snapshots of this simulation in Figure 4, together with the equivalent ones for the case of $R = 100\,\mu\text{m}$ droplets and given for the same non-dimensional time τ. The liquid bridge expands during the first stage of coalescence for both cases ($\tau = 0.51$). The merged droplet obtains an oblate shape along the axis of droplets initial centres ($\tau = 0.62$). We observe the higher relative curvature of the merged droplet for the 100 μm case. Such a droplet exhibits a higher degree of expansion per radius compared to the case of microdroplets. In both cases, the liquid bridge hits upon the superhydrophobic surface and the merged droplet expands its contact area up to a certain point ($\tau = 1.28$). During this stage, the shape of the microdroplet does not experience some of the features that appear in the larger droplet case, such as oscillations of the interface and formations of dimple shapes. The latter can be explained by the existence of strong inertial forces that counteract the capillary forces at the interface. The effect of capillarity is enhanced at areas of the interface where the droplet is experiencing local maxima of the curvature. In contrast, inertia does not produce the same effect on the microdroplet, in which case the curvature is retained lower. At $\tau = 1.75$, the mass of the droplet moves from the x-direction towards the *y*- and *z*-directions (see Figure 4), with that movement being impeded by the existence of the solid surface. Furthermore, the droplet begins retracting from the surface. The interaction of momentum in the *z*-direction with the surface will create an upwards motion that will reach a maximum vertical velocity around $\tau = 2.3$ as it is shown in Figure 5. It is interesting to point out that the peak velocity is attained slightly earlier for the microdroplet case. Subsequently, the merged droplet experiences deceleration, while the contact area with the surface continues to reduce until the moment the droplet jumps. We note that the detachment is experienced earlier by the larger droplet at $\tau = 2.5$, while for the microdroplet, it takes place at $\tau = 2.7$. Specifically, a deceleration of 15% is observed for the latter while the jumping velocity of the larger droplet is only decreased by 4%. The deceleration phase spans until moments after jumping, because of the existence of a low-pressure area beneath the merged droplet and due to oscillations. Following that phase, the jumping droplet has obtained its travelling velocity through air. This velocity differs for the two cases, as in the case of larger droplets, the gravity and inertia will dictate the

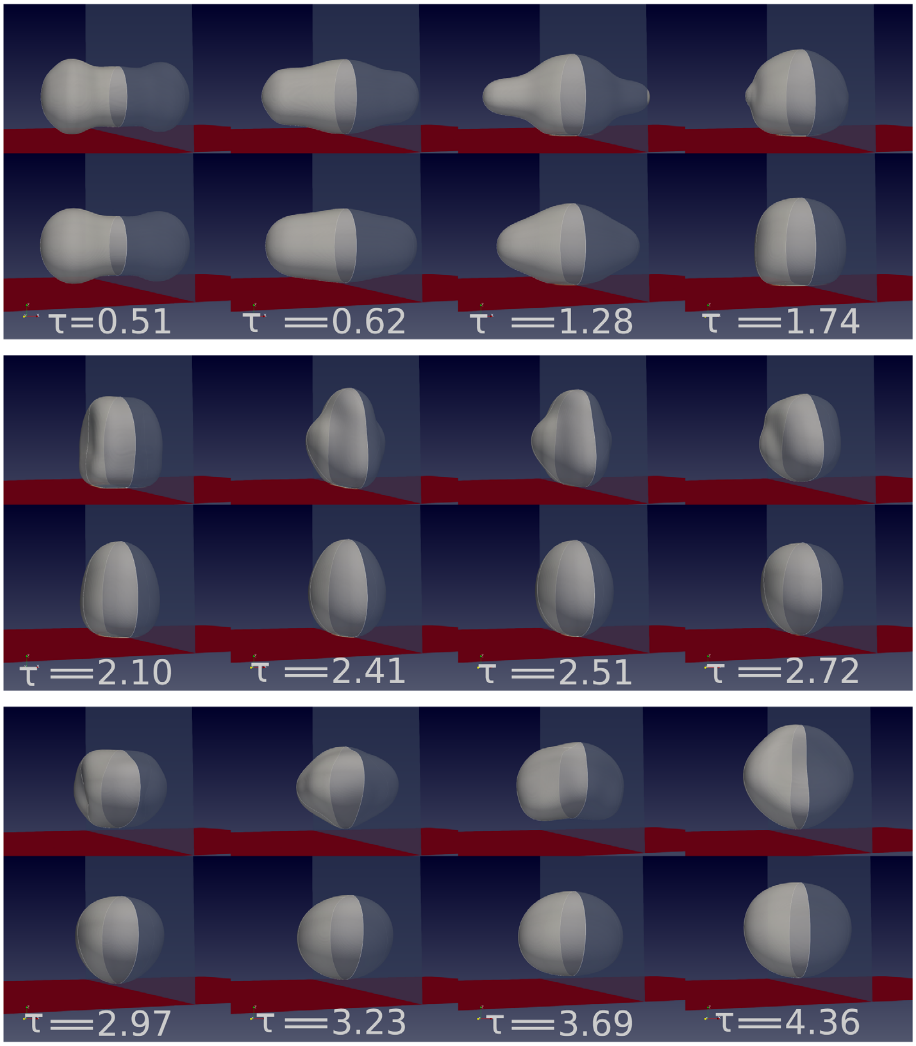

FIGURE 4 Comparison between different stages of jumping of droplets with an initial radius of $R = 100\ \mu m$ (top row in subfigures) and $R = 1\ \mu m$ (bottom row in subfigures). The snapshots are made at instants that correspond to equivalent non-dimensional capillary-inertial time-scales. Oscillations are less apparent in the microdroplet case. We also note the absence of high-curvature locations in comparison to the $R = 100\ \mu m$ case.

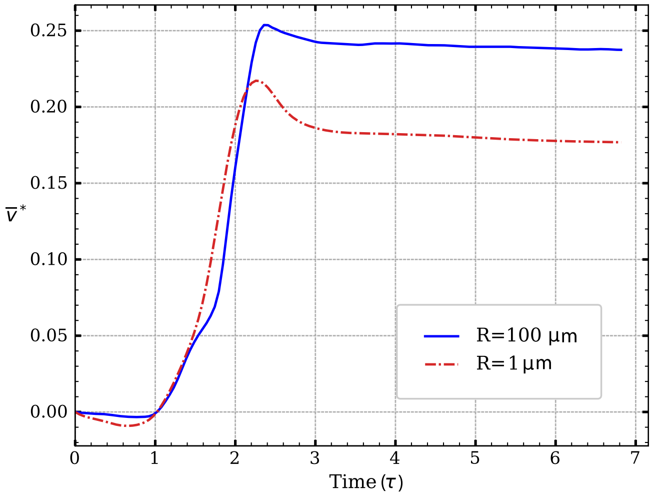

FIGURE 5 Evolution of the vertical velocity for the droplets with $R = 100\ \mu m$ and $R = 1\ \mu m$. Time and velocity are normalized with the capillary-inertial scales. There is a decrease in the jumping velocity for the microdroplet, while the latter is launched at a later moment than the larger one.

movement, while for the microdroplets, the viscous forces are most dominant. Note that the effect of viscous forces is not equally dominant in the jumping of the two types of droplets, since the time scales are dependent on $R^{3/2}$. In such cases, the accuracy of the numerical framework becomes particularly important because it is what makes it possible for us to gain an understanding of the dissipative behaviour during and following the jumping process.

It is also useful to look at the energy budget of the process. Figure 6A,B depict the total kinetic energies during the jumping of microdroplets and larger droplets, respectively. For each case, the kinetic energies of the velocity components are also presented in order to understand in which direction the greater amount of the released surface energy has been absorbed. In addition, the reduction in the surface energy, which is given to the merged droplet due to the surface tension of the water–air interface, is shown in Figure 7. At the beginning of the merging process, the majority of the

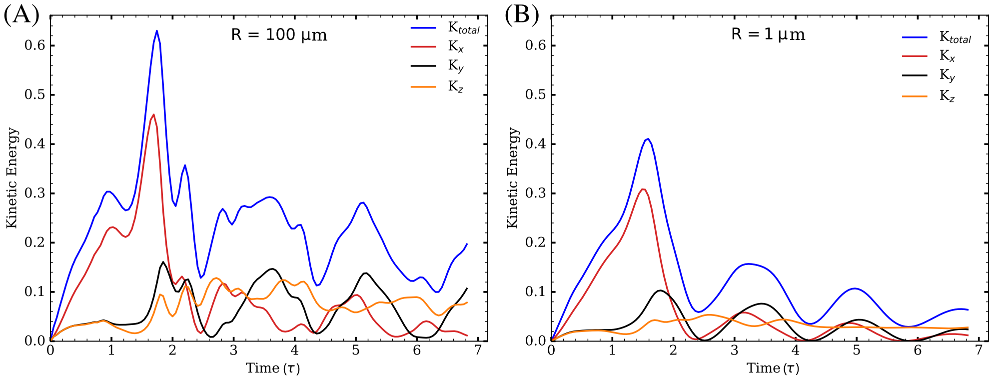

FIGURE 6 Total kinetic energies (K_{total}) in the system normalized by the available released surface energy. The kinetic energies computed by the direction components of the velocity (K_i) are superimposed. Figure (A) corresponds to the $R = 100$ μm droplets case and figure (B) to droplets of $R = 1$ μm. The maximum percentage of the available energy that was given as the kinetic energy in the system for the microdroplets is significantly reduced compared to that in the larger droplet case.

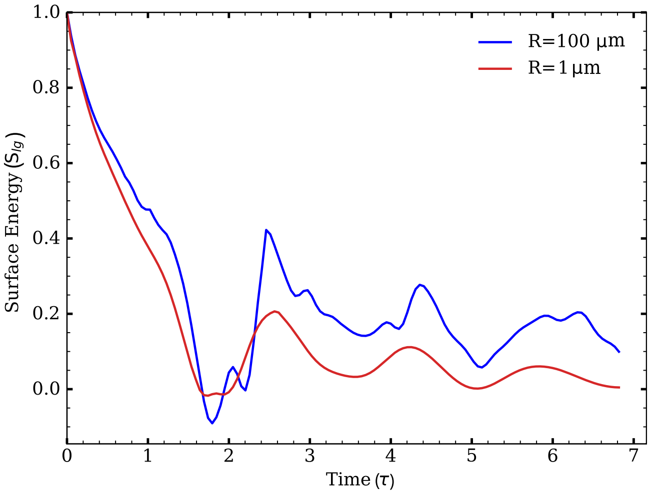

FIGURE 7 Surface energies (S_{lg}) for the $R = 100$ μm and $R = 1$ μm cases. The energies are computed from the interface area of the water–air interaction and are normalized by the available released surface energy for each case. A higher percentage of the available energy has been released during the early jumping stage for $R = 1$ μm droplets.

released surface energy is transformed to kinetic energy in the *x*-direction. A microdroplet is somewhat less efficient in this process than a larger one, as a smaller percentage of its available energy transforms to the kinetic energy. After the droplet goes through the initial stage of expansion in the x-direction until $\tau = 1.3$ and then rapidly retracts up to $\tau = 2.0$, the kinetic energy in the system is experiencing a steep decrease. Such an observation implies that the energy in the system is stored as the surface energy at either the interface or at the contact area with the solid surface. It is noted that the merged microdroplet during this process has experienced a higher surface energy release in the initial stage of its expansion on the superhydrophobic surface. This suggests that either the energy could not be stored at the surface due to extreme capillary forces at high curvature areas or that it has already dissipated due to viscosity after the initial phase, during which the released surface energy is given as momentum in the system. Therefore, viscosity is one of the assisting reasons that causes the velocity of the capillary wave to decrease, before the latter could reach the low curvature area of the interface.

Even though the process as a whole is adhering to the capillary-inertial regime by following the corresponding velocity and time scales, the higher dissipated energy in the microdroplet case could be attributed to either viscous forces or the effect of the surface tension that limits inertia at high curvature areas of the interface. An explanation for the latter would be that the peak capillary forces do not scale with *R* as the radius of the droplets decreases, but with a power of n^{-1}, where $n > 1$.

For the final energy that will be converted to upwards motion, the efficiency is given by the percentage of the available energy that is transformed to the translational kinetic energy of the merged droplet in the vertical direction. The available energy in the system is the difference between the energy of the initial interface area of the coalescing droplets and the reduced surface energy of the jumping merged droplet when the latter finally obtains a spherical shape. For the case of the initial droplets of 100 μm, the energy conversion to the jumping motion was calculated as 4.8%, while for the $R = 1$ μm case, it was obtained to be 2.8%. For even smaller initial droplets of 0.5 μm, the conversion was 2.8%. The results signify that the efficiency is markedly decreased for the jumping of microdroplets, even though they still manage to be expelled from the surface. Comparing the behaviour of the kinetic and surface energies in Figures 6 and 7, it is suggested that during the initial stage of merging, when the liquid bridge expands and after its impingement on the surface, the merged droplet extends its contact area with the superhydrophobic surface. As a result, and comparing the two cases, the larger droplets receive a higher percentage of the released surface energy in the form of the total kinetic energy.

So far, we have established that microdroplets coalesce and can effectively jump, although they do it with a reduced jumping velocity and energy conversion rate. Observations from these simulations may appear contradicting to some of the previous experimental and numerical results, which emphasize that a viscous cut-off is causing the merged droplet to adhere to the surface.[1,51,52] The Ohnesorge number (Oh), given by Equation (6), compares the viscous forces with the geometric mean of inertial and capillary forces.

$$\text{Ohnesorge Oh} = \frac{\mu}{\rho\sigma R} \sim \frac{\text{Viscous forces}}{\sqrt{\text{Inertia} \cdot \text{Capillary}}} \tag{6}$$

This nondimensional number shows that, for the viscosity to completely dampen any effects arising from high capillary forces during coalescence, it has to be comparable to both surface tension and inertia. The Weber number (We), given in Equation (7), informs us of the relative importance of inertial forces to capillary ones.

$$\text{Weber We} = \frac{\rho V^2 R}{\sigma} \sim \frac{\text{Inertia}}{\text{Capillary}} \tag{7}$$

As it is seen in both our work and in previous studies, in the capillary-inertial regime, the process follows a certain scaling with regards to the velocity and time. With a constant normalized jumping velocity $\overline{v}^*_{\text{jump}}$, we have $\text{We} = \overline{v}^{*\,2}_{\text{jump}}$, which is also a constant value. If $\overline{v}^*_{\text{jump}}$ is approximately 0.24, as it has been observed for droplets larger than 20 μm, then the Weber number becomes We = 0.058. Such a low value shows the dominance of capillary forces in this regime and that the two forces scale the same way with regards to the governing length scale of the system. The observation further suggests that when the length scale is reduced and a decrease in the non-dimensional velocity is observed, the Weber number will decrease even further.

To complete this analysis, a thorough understanding is required of the role of Reynolds (Re) and capillary (Ca) non-dimensional numbers, which are defined as in Equations (8) and (9), respectively.

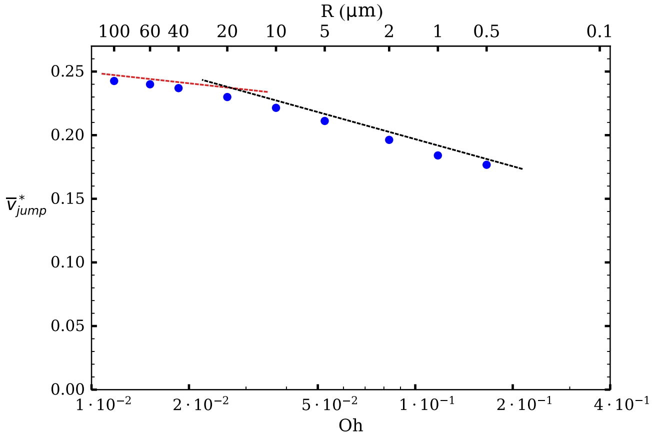

FIGURE 8 Normalized jumping velocities for the simulations involving droplets of varying initial radius as a function of the Ohnesorge number (log-scale). The red and black dashed lines represent the trends (i.e., different slopes) on a logarithmic scale for the jumping velocity of the larger- and microdroplets, respectively. We note that the jumping speed declines faster for droplets with radii corresponding to the Ohnesorge number of 0.03 and greater (initial droplets of 20 μm as the onset of this behaviour) in comparison to the larger droplets.

$$\text{Reynolds Re} = \frac{\rho V R}{\mu} \sim \frac{\text{Inertia}}{\text{Viscous forces}} \tag{8}$$

$$\text{Capillary Ca} = \frac{\mu V}{\sigma} \sim \frac{\text{Viscous forces}}{\text{Capillary}} \tag{9}$$

In the case of the jumping microdroplet with an initial radius of 1 μm, the jumping velocity was $\overline{v}^*_{\text{jump}} = 0.185$. This translates to Re = 1.4 and Ca = 0.024,which for the average velocity of the system indicates that the inertial forces may still be of higher importance than the viscous ones. It also indicates that at these length scales, the two types of forces are of comparable magnitude. On the other hand, the capillary forces are still some 40 times greater than the viscous ones and dictate the behaviour during coalescence. Since the Ohnesorge number can be expressed as $\text{Oh} = \sqrt{\frac{\text{Ca}}{\text{Re}}}$, we argue that even though a cut-off radius has been observed in previous studies, and as long as the viscous forces are not dominant, the capillary forces will overcome any effects from the viscosity. The analysis suggests that a significant part of the surface energy will be given as the kinetic energy to the system, and the coalesced droplets will eventually jump. For these reasons, as it will be shown later in the article, we interpret the notion of a cut-off radius to be caused by the interaction of a droplet with a superhydrophobic surface and the relative size of the microdroplets to the microstructures or nanostructures that exist on these surfaces.

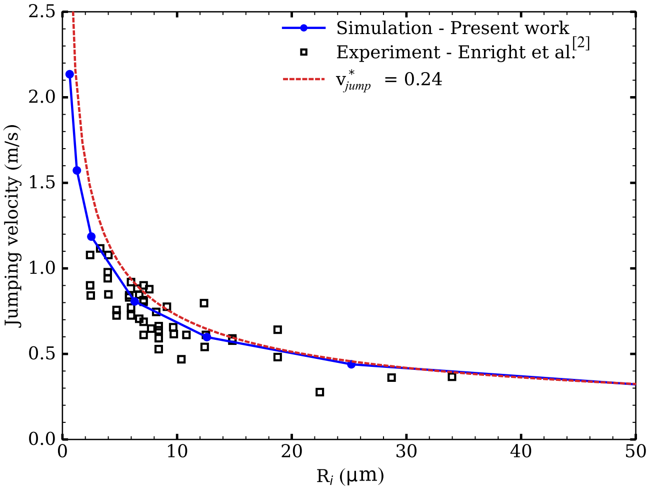

FIGURE 9 Jumping velocities for merged droplets of different radius. The simulation results are compared to the experimental data for jumping droplets by Enright et al.[2] The dashed curve represents a constant jumping velocity of 0.24 U_{CI}.

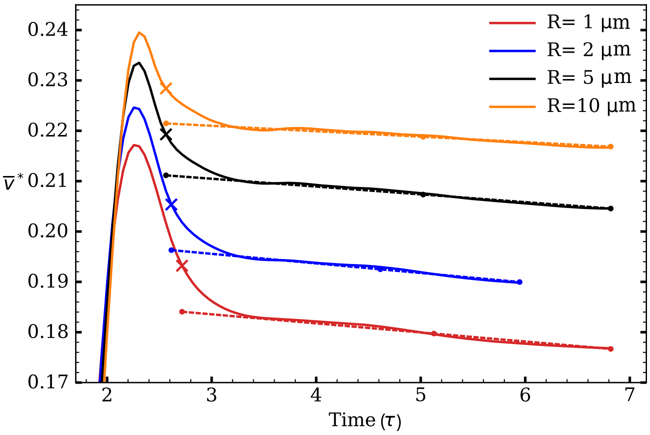

FIGURE 10 Normalized jumping velocities for four different microdroplets obtained by the simulations. The solid lines represent the average vertical velocity, and the crosses indicate the jumping moments. The dashed lines show the linear decrease in the velocity after detachment. The velocity is extrapolated backwards to the point of detachment, giving the jumping velocity.

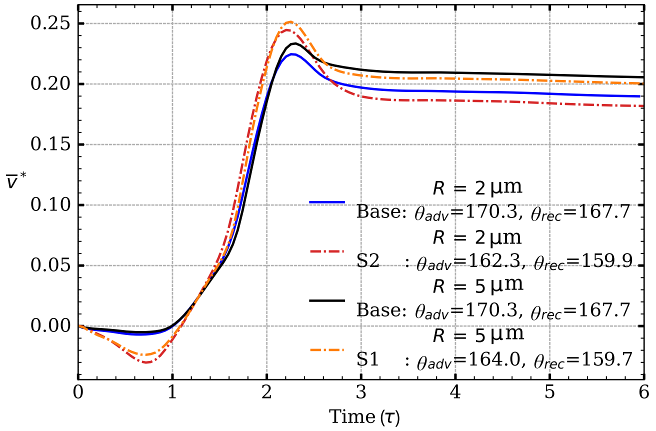

FIGURE 11 Simulations of jumping of 2 and 5 μm droplets on surfaces with different wettabilities (smaller contact angles and a more pronounced hysteresis). The contact angle values correspond to the surfaces S1 and S2 in Mulroe et al.[46] The simulations were performed using the minimum radius for which jumping was observed in the experiments. The obtained results are then compared to those with the base case contact angle values.

Connecting our previous discussion on what happens at such small scales to the corresponding Ohnesorge numbers, simulations have been performed for droplets of an initial radius ranging from 0.5 to 60 μm. The obtained results for the jumping velocity are presented in Figure 8, with respect to the Ohnesorge number and with the sizes of the initial droplets indicated on the top of the figure. We note that the calculated velocities decrease as the radius decreases but observe a steeper decrease for droplets smaller than 20 μm (corresponding to the Ohnesorge number of 0.03). Additionally, we compare our results to experimental results for equivalent droplet sizes by Enright et al.[2] In Figure 9, the jumping velocity of the droplets is depicted, alongside the data from the mentioned experimental study and a curve that corresponds to a constant normalized jumping velocity of $\overline{v}^*_{\text{jump}} = 0.24$. The figure demonstrates the ability of our framework to capture the behaviour of the jumping velocity that has been observed in the experiment. The experimental results were obtained for similar advancing and receding contact angles ($\theta_{\text{adv}} \simeq 170.2^\circ$ and $\theta_{\text{rec}} \simeq 166^\circ$) with nanostructures of up to 0.82 μm on the superhydrophobic surface. The simulation results are provided with respect to the merged droplets radius as the experimental study suggested.

It is also of interest to explain how the jumping velocity is obtained from the simulations. The droplet is considered detached from the surface when all computational cells adjacent to the surface are filled with air. The evolution of the average velocity in the vertical direction is given in Figure 10, and the point of detachment is noted with an ×-symbol. The velocity is plotted for the cases of 1, 2, 5, and 10 μm of the coalescing droplets. The linear decrease in the velocity is extrapolated backwards to the moment of detachment in order to yield the considered jumping velocity, $\overline{v}^*_{\text{jump}}$, for the merged droplet. The jumping velocities presented previously in Figures 8 and 9 are extracted in the same way.

All our simulation cases of the jumping of microdroplets up to now have involved superhydrophobic surfaces with a slight hysteresis and with very high contact angles. The final part of our analysis is thus obtained by changing the surface wetting properties. We first simulate a case with a similar hysteresis but with lower advancing and receding contact angles. We then proceed by looking at the influence of a more pronounced hysteresis. For that purpose, the previously shown results (that we here term the base case) are compared with the simulations that take the contact angle values from the experimental study of Mulroe et al.[46] Two different surfaces from that work are used, termed S1 and S2, and their wetting properties differ because of changes in surface microstructure. For the surface S1, $\theta_{\text{adv}} = 164.0^\circ$ and $\theta_{\text{rec}} = 159.7^\circ$, we look at the jumping of 5 μm microdroplets, whereas for S2, $\theta_{\text{adv}} = 162.3^\circ$ and $\theta_{\text{rec}} = 159.9^\circ$, the jumping of 2 μm microdroplets is investigated. In the cited experimental work, the reported 2 and 5 μm droplets were the minimal observed sizes of droplets that indeed jumped on S1 and S2. In Figure 11, we compare the simulation results using the mentioned droplet sizes from the two surfaces with the results acquired using the surface properties of our base case simulations. During the initial stage of the process, the microdroplets on the S1 and S2 surfaces show a more pronounced adhesive behaviour when the liquid bridge expands, directing their mass towards the surface. The relaxation of the effective contact angle in the system from its initialization value, which was set as a mean of the advancing and receding angles, to the receding value for the start of coalescence, is the most probable cause of this behaviour. In addition, the centre mass of the droplets, in comparison with the base case, is located closer to the surface due to the smaller contact angle. This results in a stronger interaction of the liquid bridge with the trapped air between the bridge and the surface. When the liquid bridge impinges on the surface and the merged droplet mass is accelerated upwards, a steeper increase in the velocity is identified for the cases involving surfaces S1 and S2. This behaviour continues until it results in a higher maximum velocity. We notice this response for both the 5 μm droplets on surface S1 and for the 2 μm droplet case on S2. Such an observation is also in accordance with the previously documented behaviour, both experimentally[44,62,63] and numerically,[35,39,64] that earlier the liquid bridge hits upon a surface during its expansion phase, the higher is the reaction energy that the merged droplet will obtain. That happens either when there is a geometrical obstacle beneath the main direction of the liquid bridge expansion, or when the centre of mass of the initial droplets is brought closer to the surface (which in this case occurs because the initial contact angle value of approximately 162∘ is lower than 169∘ for the base case surface). After the peak of the upwards velocity is reached, the droplet goes through another adhesion phase with the receding behaviour, while it takes longer to detach compared to the surface of the base case simulations. When the merged droplet has eventually detached, we observe a lower average jumping velocity, but the same deceleration rate while airborne for the simulations with different surfaces. It is important to point out that for both 2 and 5 μm cases, the droplets jumped with a smaller velocity, something that can most likely be attributed to the smaller receding angle that causes dissipation of energy before the merged droplets are released.

In summary, we have shown that a carefully formulated (with respect to the governing physics) and thoroughly validated numerical framework is able to predict the jumping of droplets of a radius as small as 0.5 μm. We have compared the behaviour of such microdroplets with the jumping of larger droplets in the capillary-inertial scaling regime that follows the constant normalized jumping velocity. Finally, it has been shown that capillary forces and viscous dissipation, to a lesser extent, are indeed factors behind the lost likelihood of the jumping of microdroplets, but in the present analysis, we point out that the main reason behind the experimentally observed existence of a cut-off radius is the surface-droplet interaction with microstructures.

5 | CONCLUSIONS

In this work, we formulated and validated a numerical framework for coalescence and jumping of microdroplets (smaller than 10 μm) on superhydrophobic surfaces. The combined VOF–immersed boundary framework involves models for advancing and receding contact angles on a number of superhydrophobic surfaces with different wetting properties. We performed a series of simulations to explain variations in the behaviour of the droplets whose size is in the lower length-scale region of the capillary-inertial scaling regime. We showed that microdroplets can jump successfully, but, as compared to the jumping of larger droplets (∼100μm), they do this with a decreased normalized jumping velocity and a smaller degree of the released surface energy converted to the kinetic energy of an upwards movement.

Our temporal and spatial convergence studies motivate using 40 cells per initial droplet radius and a constant time step that assures that we always work with a CFL smaller than 0.5. In all our simulation cases, we used adaptive mesh refinement to improve accuracy near the interface and the moving contact line. The framework was further validated by presenting a good qualitative agreement with the experimental evidence for all the stages of the jumping process for $R = 288$ μm droplets.[17]

Our results showed that for 1 μm microdroplets, a smaller degree of the total energy is given as kinetic energy in the initial stage of the process, as compared to the jumping of larger droplets. During a droplet jumping process, in general, it is known that a part of the kinetic energy is returned to the surface energy and vice versa during the oscillation of a coalesced droplet. We observed that this exchange happens less efficiently in the case of microdroplets. It is possible that viscosity is an important mechanism behind dissipation, but we argue that another important reason is that the peak capillary forces at high curvature locations may not follow the capillary-inertial scaling with a droplet radius. Instead, they show an increased strength in comparison to those during the jumping of larger droplets. For the jumping of $R = 100\,\mu\text{m}$ droplets, we calculated the degree of energy conversion to an upwards movement to be approximately 5%. We showed that this number is generally reduced to a half for microdroplets.

Through an analysis of the Ohnesorge number and a comparison of the inertial and capillary forces as a function of viscosity, we concluded not only that the capillary forces are the main driving mechanism behind the microdroplets jumping process but also that inertia is still an important factor. In that sense, we note that the Reynolds number is greater than unity, calculated with the average jumping velocity at $R = 100\,\mu\text{m}$. Our findings are in contrast with some previous studies, which suggest that viscous forces are behind the existence of a cut-off region (a set of values for which droplets of certain sizes can jump). We argue instead that the dissipation that has been observed at such scales in previous experimental studies is due to interactions with microstructures on the surface.

We also presented the simulations of jumping of microdroplets with an initial radius of as small as $R = 0.5\,\mu\text{m}$ and compared their jumping velocities with the experimental findings of another research group.[2] The simulations accurately reproduced the experimental observations even in the case of such small droplets.

Finally, we looked at the fundamentals of the microdroplet jumping process when a more pronounced hysteresis of contact angles is present not only on superhydrophobic surfaces but also on surfaces with a smaller degree of superhydrophobicity. For that purpose, we ran the simulations of 2 and 5 μm droplets and proved that, by considering the superhydrophobic surface as flat and correctly assigning the corresponding contact angles, the droplets will manage to jump with a reduction in their velocity and small variations in the jumping process (mostly in the form of a more pronounced adhesive behaviour during the expansion of a liquid bridge).

NOMENCLATURE

$\hat{\mathbf{n}}$	unit interface normal vector (−)
$\mathbf{f}_{SF}$	surface tension body force ($\text{kg} \cdot \text{m}^{-2} \cdot \text{s}^{-2}$)
$\mathbf{n}$	interface normal vector (m^{-1})
$\mathbf{v}$	velocity ($\text{m} \cdot \text{s}^{-1}$)
$\mathbf{v}_{wall}$	slip velocity at wall ($\text{m} \cdot \text{s}^{-1}$)
K_i	normalized kinetic energy in direction i (−)
K_{total}	normalized total kinetic energy normalized (−)
S_{lg}	normalized surface energy in the liquid–gas interface (−)
$\bar{v}^*$	averaged normalized vertical velocity of droplet (−)
$\bar{v}^*_{\text{jump}}$	normalized jumping velocity of droplet (−)
Ca	capillary number (−)
g	gravitational acceleration ($\text{m} \cdot \text{s}^{-2}$)
n_{w}	normal wall direction (m)
Oh	Ohnesorge number (−)
p	pressure ($\text{kg}{\cdot}\text{m}^{-1} \cdot \text{s}^{-2}$)
R	radius of initial droplets (m)
R_{c}	radius of merged droplet (m)
Re	Reynolds number (−)
t	time (s)
U_{CI}	normalized capillary-inertial velocity (−)
We	Weber number (−)

Greek letters

α	volume fraction (−)
$\Delta\tau$	normalized time step (−)
Δt	time step (s)
Δx	cell size (m)
κ	interface curvature (m^{-1})
λ	slip length (m)
τ	normalized time (−)
τ_{CI}	normalized capillary-inertial time (−)
μ	dynamic viscosity ($\text{kg} \cdot \text{m}^{-1} \cdot \text{s}^{-1}$)
ρ	density ($\text{kg} \cdot \text{m}^{-3}$)
σ	surface tension ($\text{kg} \cdot \text{s}^{-2}$)
θ_{adv}	advancing contact angle (°)
θ_{rec}	receding contact angle (°)

Abbreviations

CFL	Courant number
CICSAM	compressive interface capturing scheme for arbitrary meshes
CSF	continuum surface force
SIMPLEC	semi-implicit method for pressure linked equations-consistent
VOF	volume of fluid

AUTHOR CONTRIBUTIONS

Konstantinos Konstantinidis: Conceptualization; data curation; formal analysis; investigation; methodology; software; validation; writing – original draft; writing – review and editing. **Johan Göhl:** Formal analysis; methodology; software; supervision; writing – review and editing. **Andreas Mark:** Formal analysis; methodology;

software; supervision; writing – review and editing. **Srdjan Sasic:** Conceptualization; formal analysis; funding acquisition; investigation; methodology; project administration; supervision; validation; writing – review and editing.

ACKNOWLEDGEMENTS

This work has been financed by the Swedish Research Council (Vetenskapsrådet, Dnr 2019-04969). The authors would like to acknowledge that the computations and handling of data were enabled by resources provided by the Swedish National Infrastructure for Computing (SNIC), partially funded by the Swedish Research Council through grant agreement no. 2018-05973.

CONFLICT OF INTEREST

The authors declare that there is no conflict of interests from this work.

DATA AVAILABILITY STATEMENT

The data of this study are available upon request from the corresponding author.

ORCID

Konstantinos Konstantinidis https://orcid.org/0000-0002-4214-6337

REFERENCES

[1] J. B. Boreyko, C. H. Chen, *Phys. Rev. Lett.* **2009**, *103*, 2.
[2] R. Enright, N. Miljkovic, J. Sprittles, K. Nolan, R. Mitchell, E. N. Wang, *ACS Nano* **2014**, *8*, 10352.
[3] S. A. Kulinich, M. Farzaneh, *Langmuir* **2009**, *25*, 8854.
[4] H. Wang, L. Tang, X. Wu, W. Dai, Y. Qiu, *Appl. Surf. Sci.* **2007**, *253*, 8818.
[5] L. B. Boinovich, A. M. Emelyanenko, *Mendeleev Commun.* **2013**, *23*, 3.
[6] S. Farhadi, M. Farzaneh, S. A. Kulinich, *Appl. Surf. Sci.* **2011**, *257*, 6264.
[7] N. Miljkovic, R. Enright, E. N. Wang, *J. Heat Transfer* **2013**, *135*, 111004.
[8] N. Miljkovic, R. Enright, Y. Nam, K. Lopez, N. Dou, J. Sack, E. N. Wang, *Nano Lett.* **2013**, *13*, 179.
[9] K. M. Wisdom, J. A. Watson, X. Qu, F. Liu, G. S. Watson, C.-H. Chen, *Proc. Natl. Acad. Sci. U. S. A.* **2013**, *110*, 7992.
[10] D. Maggiolo, M. Seemann, H. Thunman, O. Santos, A. Larsson, S. Sasic, H. Ström, *AIChE J.* **2019**, *65*, 317.
[11] S. P. Dalawai, M. A. Saad Aly, S. S. Latthe, R. Xing, R. S. Sutar, S. Nagappan, C. S. Ha, K. Kumar Sadasivuni, S. Liu, *Prog. Org. Coat.* **2020**, *138*, 105381.
[12] C. Yu, S. Sasic, K. Liu, S. Salameh, R. H. Ras, J. R. van Ommen, *Chem. Eng. Res. Des.* **2020**, *155*, 48.
[13] Q. Wang, X. Yao, H. Liu, D. Quéré, L. Jiang, *Proc. Natl. Acad. Sci. U. S. A.* **2015**, *112*, 9247.
[14] C. Lv, P. Hao, Z. Yao, Y. Song, X. Zhang, F. He, *Appl. Phys. Lett.* **2013**, *103*, 1.
[15] G. S. Watson, M. Gellender, J. A. Watson, *Biofouling* **2014**, *30*, 427.
[16] S. Nishimoto, B. Bhushan, *RSC Adv.* **2013**, *3*, 671.
[17] X. Yan, L. Zhang, S. Sett, L. Feng, C. Zhao, Z. Huang, H. Vahabi, A. K. Kota, F. Chen, N. Miljkovic, *ACS Nano* **2019**, *13*, 1309.
[18] C. Lv, P. Hao, X. Zhang, F. He, *ACS Nano* **2015**, *9*, 12311.
[19] C. Lv, P. Hao, Z. Yao, F. Niu, *Langmuir* **2015**, *31*, 2414.
[20] X. Chen, R. S. Patel, J. A. Weibel, S. V. Garimella, *Sci. Rep.* **2016**, *6*, 18649.
[21] D. Quéré, *Annu. Rev. Mater. Res.* **2008**, *38*, 71.
[22] E. B. Dussan, *Annu. Rev. Fluid Mech.* **1979**, *11*, 371.
[23] P. G. de Gennes, *Rev. Mod. Phys.* **1985**, *57*, 827.
[24] D. Legendre, M. Maglio, *Comput. Fluids* **2015**, *113*, 2.
[25] J. H. Snoeijer, B. Andreotti, *Annu. Rev. Fluid Mech.* **2013**, *45*, 269.
[26] K. Wang, Q. Liang, R. Jiang, Y. Zheng, Z. Lan, X. Ma, *Langmuir* **2017**, *33*, 6258.
[27] Y. Wang, P. Ming, *Phys. Fluids* **2019**, *31*, 122108.
[28] F. Liu, G. Ghigliotti, J. J. Feng, C. H. Chen, *J. Fluid Mech.* **2014**, *752*, 39.
[29] Y. Cheng, J. Xu, Y. Sui, *Int. J. Heat Mass Transfer* **2016**, *95*, 506.
[30] Y. Nam, H. Kim, S. Shin, *Appl. Phys. Lett.* **2013**, *103*, 161601.
[31] Y. Chen, Y. Lian, *Phys. Fluids* **2018**, *30*, 112102.
[32] X. Chen, J. Lu, G. Tryggvason, *Phys. Fluids* **2019**, *31*, 052107.
[33] F. Chu, X. Wu, B. Zhu, X. Zhang, *Appl. Phys. Lett.* **2016**, *108*, 194103.
[34] F. Chu, Z. Yuan, X. Zhang, X. Wu, *Int. J. Heat Mass Transfer* **2018**, *121*, 315.
[35] H. Vahabi, W. Wang, J. M. Mabry, A. K. Kota, *Sci. Adv.* **2018**, *4*, eaau3488.
[36] Z. Yuan, R. Wu, X. Wu, *Int. J. Heat Mass Transfer* **2019**, *135*, 345.
[37] J. Wasserfall, P. Figueiredo, R. Kneer, W. Rohlfs, P. Pischke, *Physical Review Fluids* **2017**, *2*, 1.
[38] R. Attarzadeh, A. Dolatabadi, *Phys. Fluids* **2017**, *29*, 012104.
[39] Y. Shi, G. H. Tang, H. H. Xia, *Int. J. Heat Mass Transfer* **2015**, *88*, 445.
[40] X. Liu, P. Cheng, *Int. Commun. Heat Mass Transfer* **2015**, *64*, 7.
[41] Z. Liang, P. Keblinski, *Appl. Phys. Lett.* **2015**, *107*, 143105.
[42] S. Gao, Q. Liao, W. Liu, Z. Liu, *J. Phys. Chem. C* **2018**, *122*, 20521.
[43] F. F. Xie, G. Lu, X. D. Wang, D. Q. Wang, *Langmuir* **2018**, *34*, 11195.
[44] R. Wen, S. Xu, D. Zhao, Y. C. Lee, X. Ma, R. Yang, *ACS Appl. Mater. Interfaces* **2017**, *9*, 44911.
[45] H. Cha, C. Xu, J. Sotelo, J. M. Chun, Y. Yokoyama, R. Enright, N. Miljkovic, *Physical Review Fluids* **2016**, *1*, 064102.
[46] M. D. Mulroe, B. R. Srijanto, S. F. Ahmadi, C. P. Collier, J. B. Boreyko, *ACS Nano* **2017**, *11*, 8499.
[47] T. Mouterde, T. V. Nguyen, H. Takahashi, C. Clanet, I. Shimoyama, D. Quéré, *Physical Review Fluids* **2017**, *2*, 1.
[48] R. Enright, N. Miljkovic, N. Dou, Y. Nam, E. N. Wang, *J. Heat Transfer* **2013**, *135*, 091304.
[49] T. Mouterde, G. Lehoucq, S. Xavier, A. Checco, C. T. Black, A. Rahman, T. Midavaine, C. Clanet, D. Quéré, *Nat. Mater.* **2017**, *16*, 658.

[50] P. Lecointre, T. Mouterde, A. Checco, C. T. Black, A. Rahman, C. Clanet, D. Quéré, *Physical Review Fluids* **2019**, *4*, 24.
[51] X. Liu, P. Cheng, X. Quan, *Int. J. Heat Mass Transfer* **2014**, *73*, 195.
[52] S. Farokhirad, J. F. Morris, T. Lee, *Phys. Fluids* **2015**, *27*, 102102.
[53] A. Mark, R. Rundqvist, F. Edelvik, *Fluid Dynamics and Materials Processing* **2011**, *7*, 241.
[54] J. U. Brackbill, D. B. Kothe, C. Zemach, *J. Comput. Phys.* **1992**, *100*, 335.
[55] J. Göhl, A. Mark, S. Sasic, F. Edelvik, *Int. J. Multiphase Flow* **2018**, *109*, 164.
[56] J. P. Van Doormaal, G. D. Raithby, *Numerical heat transfer* **1984**, *7*, 147.
[57] M. M. Francois, S. J. Cummins, E. D. Dendy, D. B. Kothe, J. M. Sicilian, M. W. Williams, *J. Comput. Phys.* **2006**, *213*, 141.
[58] P. Bartholomew, F. Denner, M. H. Abdol-Azis, A. Marquis, B. G. van Wachem, *J. Comput. Phys.* **2018**, *375*, 177.
[59] C. M. Rhie, W. L. Chow, *AIAA J.* **1983**, *21*, 1525.
[60] A. Mark, B. G. van Wachem, *J. Comput. Phys.* **2008**, *227*, 6660.
[61] S. Afkhami, S. Zaleski, M. Bussmann, *J. Comput. Phys.* **2009**, *228*, 5370.
[62] K. Wang, Q. Liang, R. Jiang, Y. Zheng, Z. Lan, X. Ma, *RSC Adv.* **2016**, *6*, 99314.
[63] Q. Peng, X. Yan, J. Li, L. Li, H. Cha, Y. Ding, C. Dang, L. Jia, N. Miljkovic, *Langmuir* **2020**, *36*, 9510.
[64] D. Lu, M. Zhao, H. Zhang, Y. Yang, Y. Zheng, *Langmuir* **2020**, *36*, 5444.

How to cite this article: K. Konstantinidis, J. Göhl, A. Mark, S. Sasic, *Can. J. Chem. Eng.* **2022**, 1. https://doi.org/10.1002/cjce.24591